Spectroscopic characterization of 1450 nm semiconductor pump laser structures for Raman amplifiers

S. B. Constant, S. Tomić, D. Lock, T. E. Sale, S. J. Sweeney et al.

Citation: J. Appl. Phys. **93**, 9446 (2003); doi: 10.1063/1.1575499
View online: http://dx.doi.org/10.1063/1.1575499
View Table of Contents: http://jap.aip.org/resource/1/JAPIAU/v93/i12
Published by the American Institute of Physics.

Spectroscopic characterization of 1450 nm semiconductor pump laser structures for Raman amplifiers

S. B. Constant, S. Tomić, D. Lock, T. E. Sale, S. J. Sweeney, and T. J. C. Hosea[a)]
Department of Physics, University of Surrey, Guildford, Surrey GU2 7XH, United Kingdom

(Received 18 November 2002; accepted 21 March 2003)

In order to characterize various different epilayer designs for semiconductor Raman amplifier pump lasers, combined electromodulated reflectance (ER) and photoluminescence (PL) studies were performed on wafer samples of InP / InGaAsP / InGaAsP edge-emitter laser structures in the infrared spectral region. Information about the quantum well (QW) transitions is obtained primarily from the ER, with additional corroboration provided by the PL. The ER spectra are fitted with a line shape model to obtain the ground-state and higher-order QW transition energies, which are found to agree well with theoretically calculated values. The ER spectra also provide the waveguide core and barrier compositions and built-in electric fields in the laser structures. The information provided by ER studies on the prefabrication wafers is found to corroborate well with diagnostic spontaneous emission measurements performed on actual laser devices fabricated from the same wafer batches.
 [DOI: 10.1063/1.1575499]

I. INTRODUCTION

Although there has been interest for some time in exploiting the Raman effect to amplify telecommunication signals,[1] the development of erbium-doped fibre amplifiers (EDFAs) at the beginning of the 1990s slowed down this research. Since the emergence of the internet, however, transmission capacity demands have increased very rapidly and, as systems seek to make use of wider optical bandwidths, EDFA technology has started to reach its limits. EDFAs are typically restricted to a narrow band from 1530 to 1580 nm, whereas the transmission window in low-loss silica fibers can extend far beyond this.[1] The Raman amplifier relies upon phonon scattering in silica optical fiber to boost optical signals. Unlike EDFAs or other rare-earth-ion-based fibers, the gain band is not fixed by the energy levels of the dopant ions but depends upon the wavelength of the pump lasers, with ~100 nm offset between the pump and peak gain wavelengths (for instance ~1450 nm pumps are used to produce gain at 1550 nm). This makes it possible to amplify any wavelength by selecting the right pumping wavelength, or a combination of pump wavelengths to cover a wide band. By varying the pump power at each of a number of pump wavelengths one can produce a reasonably flat gain profile. Of further advantage is the fact that it is possible to obtain amplification in existing silica fibers, thus decreasing the costs of implementation. This is particularly useful for preamplification: if the pump lasers are propagated along a fiber with the data transmission, the data signal can be amplified as it travels, and so is less susceptible to noise. Counterpropagation provides additional advantage by amplifying the signal most when it is weakest and by providing immunity to high frequency noise from the pump laser. This technique allows for longer transmission spans or less sophisticated, and so cheaper, receivers to be employed. Raman scattering is a very weak effect, requiring pump lasers with high power (typically 0.5–2 W across the pump wavelength range) to produce sufficient gain and long interaction lengths (typically many kilometers).

We have recently designed several possible structures for such Raman pump lasers. As part of a careful exploration of designs we have performed a range of investigations, from wafer characterization through to device fabrication and performance studies. We report here a study of the ability of various optical techniques to characterize prefabrication Raman pump laser structure wafers. The primary method employed is electromodulated reflectance (ER), which measures the fractional change in sample reflectivity, $\Delta R/R$, due to external modulation of the sample dielectric function by an applied ac field. We use a form of ER which could be employed as a tool for characterizing structures early in the manufacturing process, and which needs no direct electrical contact to be fabricated onto the sample. It is well known that modulated reflectance techniques such as ER can give much more information than simple reflectance (R) or photoluminescence (PL), such as the ground state, and any higher-order, transition energies of the various materials in the structure, as well as allowing e.g., layer compositions, thicknesses, and built-in electric fields to be deduced. Such on-wafer, nondestructive, prefabrication testing can be useful to growers in deciding if batches of wafers can be processed to make good quality devices, or, if the results show poor characteristics, regrown, without incurring too much expense or loss of time. The ER method described here is essentially nondestructive as it only requires a very slight contact of a separate flat transparent top electrode onto the surface of the sample, which could then be processed later into working devices, if desired.

Here, ER spectroscopic studies are performed on pieces of wafers from four different edge-emitter laser structures designed to be Raman pumps operating near 1450 nm. The ER spectra are analyzed in several ways to obtain: (1) the

a)Electronic mail: j.hosea@surrey.ac.uk

TABLE I. Summary of the $In_{1-xw}Ga_{xw}As_{yw}P_{1-yw}$ QW and $In_{1-xb}Ga_{xb}As_{yb}P_{1-yb}$ barrier structure. For all samples the unstrained waveguide core is designed to have a band gap wavelength of $\sim 1.1\ \mu$m , the same as the barrier, except in sample C where the barriers are tensilely strained. The values denoted by $^{(k)}$ are those used in the final theoretical $\mathbf{k}\cdot\mathbf{p}$ calculations of the QW transition energies (Sec. V). In these calculations, nominal compositions (denoted by $^{(n)}$) were used for the QW, but the barrier compositions were those adjusted using the barrier band gap energies obtained from the ER experiments. To achieve a match with experiment, only the QW thickness L_Z was allowed to vary in the model, within the limits of the TEM uncertainties (figures in parentheses) $^{n}=$ nominal values, $^{t}=$ TEM measurements, $^{e}=$ deduced from ER results, and $^{k}=$ values used in the $\mathbf{k}\cdot\mathbf{p}$ model

	QW			Barrier/waveguide-core		
Sample	Width (Å)	Strain (%)	Composition (xw,yw)	Width (Å)	Strain (%)	Composition (xb,yb)
A	$40^{(n)}$ $32(9)^{(t)}$ $40^{(k)}$	$1.0^{(nk)}$	$0.263, 0.874^{(nk)}$	$100^{(nk)}$ $119(9)^{(t)}$	$0^{(nk)}$	$0.146, 0.318^{(n)}$ $0.157, 0.343^{(ek)}$
B	$50^{(n)}$ $46(9)^{(t)}$ $55^{(k)}$	$1.0^{(nk)}$	$0.238, 0.821^{(nk)}$	$100^{(nk)}$ $115(9)^{(t)}$	$0^{(nk)}$	$0.146, 0.318^{(n)}$ $0.136, 0.297^{(ek)}$
C	$50^{(n)}$ $46(9)^{(t)}$ $53^{(k)}$	$0.9^{(nk)}$	$0.256, 0.848^{(nk)}$	Waveguide Core $100^{(nk)}$ $110(9)^{(t)}$	$0^{(n)}$ $-0.28^{(nk)}$	$0.190, 0.414^{(n)}$ $0.174, 0.379^{(ek)}$ $0.190, 0.326^{(n)}$ $0.181, 0.309^{(ek)}$
D	$60^{(n)}$ $64(9)^{(t)}$ $70^{(k)}$	$1.0^{(nk)}$	$0.221, 0.785^{(nk)}$	$100^{(nk)}$ $110(9)^{(t)}$	$0^{(nk)}$	$0.146, 0.318^{(n)}$ $0.153, 0.335^{(ek)}$

active region quantum well (QW) transition energies; (2) the band gap (E_g) of the quaternary waveguide-core/barrier regions of the structures; and (3) the built-in electric fields (ε_z) in the waveguide core material. Besides corroborative PL measurements on the wafers, preliminary spontaneous emission (SE) measurements are also performed on actual devices fabricated from the same batches of wafers, and both the SE and PL results are compared with the accurate QW information provided by the ER. Theoretical calculations of the QW and barrier transition energies are also performed and compared with the ER results in order to refine growth parameters such as well widths and barrier compositions.

II. EXPERIMENTAL DETAILS

The four 1450 nm edge emitter laser structures studied (labeled A, B, C, D, here) were grown by low pressure molecular organic chemical vapor deposition (MOCVD) on InP substrates and comprise four $In_{1-xw}Ga_{xw}As_{yw}P_{1-yw}$ active-region QWs, which are $\sim 1\%$ compressively strained, of nominal widths, L_z, of: 40 Å for sample A; 50 Å for samples B and C; and 60 Å for sample D. All structures have 100 Å $In_{1-xb}Ga_{xb}As_{yb}P_{1-yb}$ barriers on either side of each QW, which for samples A, B, and D have a band gap wavelength of $\sim 1.1\ \mu$m and are lattice matched to InP. Sample C, however, has tensilely strained (-0.28%) barriers, the intention being to provide not only deeper wells but also a larger conduction band (CB) offset. This should give better electron confinement than in the other three structures and so potentially achieve a better balance between the electron and hole concentration in the QW, which in turn should help reduce Auger recombinations, which are dominated by np^2 processes.[2] In all structures, the active region is sandwiched between two thick 2500 Å InGaAsP unstrained waveguide-core (band gap $\sim 1.1\ \mu$m), and thick InP cladding layers. The structures were characterized by transmission electron microscope (TEM) measurements to determine QW and barrier layer thicknesses, as shown in Table I.

Devices were subsequently fabricated from batches of wafers grown at the same time as those used in the ER and PL studies, the only difference being that waveguide cladding and electrical contacting layers were added in a subsequent growth run. The wafers studied by optical characterization were removed from the process line before this final growth run since the thick, heavily p-doped InGaAs contact layer would strongly attenuate wavelengths shorter than 1.66 μm, so preventing optical access to the active region at the wavelengths of interest.

Figure 1 shows the experimental set up for making simultaneous ER and R measurements in air. The probe beam is supplied by a conventional tungsten–halogen lamp and monochromator arrangement [instrumental resolution full width at half maximum (FWHM) 3.4 nm] and signals detected with an InGaAs photodiode and lock-in amplifier arrangement. A piece was cleaved out of each wafer and held between two electrodes: one a grounded copper plate and the other a glass slide coated with transparent indium tin oxide (ITO), as described in detail elsewhere.[3] The ER was excited by a sinusoidal voltage applied to the transparent electrode, provided by the internal oscillator of the lock-in-amplifier (333 Hz), which was amplified to ~ 50 V by external circuitry. The resulting average ac field amplitude across the $\sim 0.5-$mm-thick samples was thus $E \sim 1$ kV/cm. Cleaving

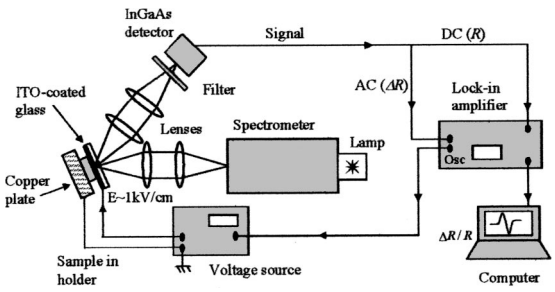

FIG. 1. Schematic of the ER experimental arrangement.

the wafer would not be necessary with an appropriate sample holding technique, so the technique can potentially be applied to wafers midprocess. Since the samples are touched only gently, our method is essentially nondestructive and samples could later be fabricated into working devices, if desired.

Corroborative PL measurements were performed in a conventional way (excitation provided by a 3 mW He–Ne laser at 632.8 nm), on the same spots on the wafers as the ER. However, an instrumental FWHM of 5.3 nm was sufficient for resolving the fairly broad emission features of the laser structures. All *R* and PL spectra were corrected for the effects of instrumental response.

In addition to the wafer characterization, preliminary device characterization was carried out by performing SE measurements on fully fabricated working laser devices. The SE was collected from a window milled into the laser substrate metallization, and passed via an optical fiber to an optical spectrum analyzer (resolution FWHM 10 nm). This enables the intrinsic SE to be determined without the distorting effects of gain and loss along the laser cavity. To minimize the effects of Ohmic heating, the lasers were driven under pulsed operation (500 ns long pulses at 1 kHz repetition). This technique is described in more detail elsewhere[4] and full device characterization results will be reported separately.

III. EXPERIMENTAL RESULTS

The results of the various optical characterization measurements are discussed next, the aim being to assess the effects of the designs (different well widths, strained and unstrained barriers, etc.) on QW and waveguide-core/barrier transition energies, as well as waveguide-core/cladding interface electric fields.

A. QW ER spectra

Figure 2 shows QW emission PL spectra of the four samples. All have a ground-state peak near ~ 0.845 eV (see Table II) except for sample B which peaks near 0.874 eV. As can be seen from Fig. 2, the PL narrows with increasing well width (FWHMs of: 53, 45, 45, and 38 meV for samples A, B, C, and D, respectively). This is consistent with monolayer fluctuations being the primary cause of this inhomogeneous broadening, since their effect would be proportionately greater in the narrower QWs.

These PL results are in good agreement with the SE device measurements (Fig. 3), where we again observe that all the main QW emission peaks are at approximately the same energy (~ 0.858 eV), except for sample B which is again higher, at ~ 0.879 eV (see Table II). All the SE peak energies are slightly higher than those of the PL (by $\sim 5 - 17$ meV). This is, we believe, due mainly to fluctuations between wafers in each of the batches, as a result of spatial nonuniformities within the MOCVD reactor. Small variations in composition are very likely, but here the QW transition is unusually sensitive to both well and barrier structure because of the quaternary alloys and thin wells: significant variation can occur in thin wells because of the short growth time and correspondingly fewer revolution periods in the planetary reactor. Whole-wafer maps of the PL peak positions showed across-wafer variations of up to ~ 12 meV, and further differences between the wafers used for the SE and PL samples of ~ 5 meV. Note that, in some cases, the SE spectra contain more structure than the PL: there are clear secondary peaks for samples B and C, corresponding to the higher-order QW transitions. It is clear from both the PL and SE results that sample B is unusual in having a higher QW ground-state transition energy. As will be seen, the ER spectra explain this anomaly.

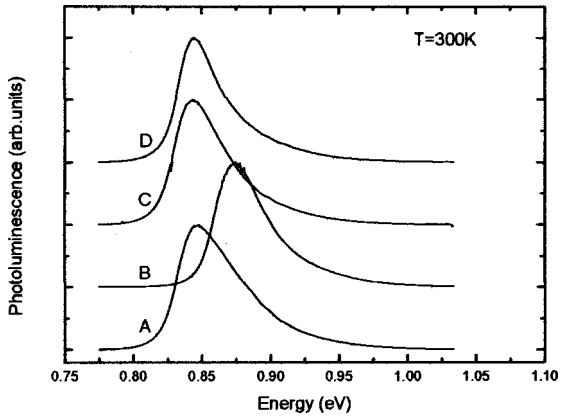

FIG. 2. Room temperature photoluminescence spectra for the four samples A, B, C, D (corrected for instrumental effects). For clarity, the base lines are offset as indicated by the ticks on the vertical axis. All spectra peak near 0.845 eV which agrees reasonably well with the specification (0.855 eV), except sample B which peaks at higher energy (0.874 eV).

The ER experiments were performed to extract more accurate and comprehensive information about the waveguide-core/barrier regions, and the QW ground-state and higher-order transition energies. Figure 4 (lower plot) shows a typical example of the ER signals obtained (here, for sample B). In order to provide an initial interpretation of these spectra we used a technique that we developed earlier which involves performing a Kramers–Kronig transformation of the ER spectrum to obtain its modulus spectrum.[5,6] Provided certain criteria are satisfied, this technique essentially removes the phase information contained in the oscillatory ER signal and transforms it into a simpler positive-definite spectrum, which has PL-like peaks near the transition energies in the ER spectrum. Figure 4 (central plot) shows such a modulus spectrum, revealing at least two low-energy QW transitions (the modulus spectra of other samples such as C and D show three clear QW modulus peaks—see Table II) and two higher-energy transitions associated with the waveguide-core/barrier layers and substrate, respectively.

The modulus spectrum is useful not only for visualizing the number and approximate energies of features in an ER spectrum, but also for providing initial parameter estimates (energies, widths, and amplitudes) for least-squares fitting of the ER spectrum with a theoretical lineshape such as Aspnes's third differential functional form (TDFF).[7] Such a fit is shown as the curve in the lower plot of Fig. 4, over the QW energy range, yielding three transition energies (vertical dashed lines). As corroboration of these results, the upper plot in Fig. 4 shows the associated SE spectrum for sample

TABLE II. Summary of the QW transition energies obtained for all samples by the various methods indicated. The figures in parentheses are the uncertainties in the last digits of the experimental measurements. The assignments (e.g., e_1hh_1) were deduced from a comparison with the theory, see Sec. V).

Sample and nominal L_Z	Method	QW transition energy (eV)			
		e_1hh_1	e_1lh_1	e_1hh_3	e_1-VB
A	PL	0.848(13)	···	···	···
	SE	0.859(14)	···	···	···
	ER modulus	0.845(14)	0.935(19)	···	···
	ER fit	0.846(1)	0.954(1)	···	1.050(2)
$L_Z=40$ Å	theory ($L_Z=40$ Å)	0.846	0.939	···	1.054
B	PL	0.874(11)	···	···	···
	SE	0.879(17)	0.929(13)	0.986(15)	1.035(10)
	ER modulus	0.861(12)	0.974(18)		···
	ER fit	0.863(1)	0.931(1)	1.001(1)	···
$L_Z=50$ Å	theory ($L_Z=55$ Å)	0.859	0.940	1.045	1.072
C	PL	0.844(1)	···	···	···
	SE	0.861(15)	0.922(15)	0.975(15)	···
	ER modulus	0.835(10)	0.910(13)	0.987(10)	···
	ER fit	0.835(1)	0.922(1)	1.038(2)	···
Tensile barrier $L_Z=50$ Å	theory ($L_Z=53$ Å)	0.832	0.926	1.036	1.063
D	PL	0.844(9)	···	···	···
	SE	0.854(15)	···	···	···
	ER modulus	0.836(10)	0.916(14)	0.971(14)	···
	ER fit	0.840(1)	0.909(1)	0.969(5)	1.044(8)
$L_Z=60$ Å	theory ($L_Z=70$ Å)	0.829	0.910	0.968	1.035

B, with peaks near the fitted ER energies. The analysis of the fitted QW transition energies is discussed fully in Sec. V.

B. Waveguide-core/barrier ER spectra

Modulated reflectance spectra also often yield signals from the bulk-like and barrier material in a QW heterostructure, which may be useful, not only for determining/checking the actual composition of, e.g., the barrier material, but also for measuring built-in electric fields.

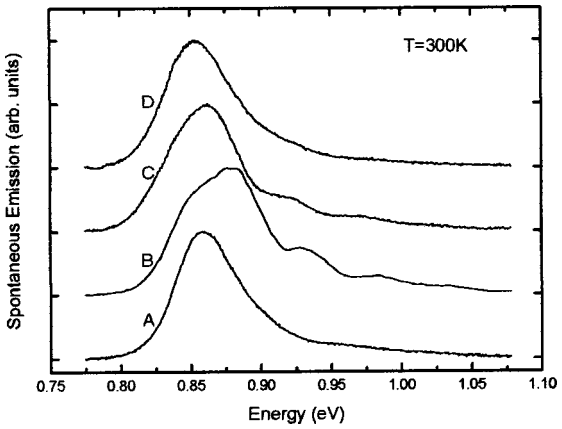

FIG. 3. Room temperature spontaneous emission spectra for fabricated devices for the four samples A, B, C, D (corrected for instrumental effects). For clarity, the base lines are offset as indicated by the ticks on the vertical axis. As in Fig. 2, all spectra peak near each other (0.858 eV), except sample B, which peaks at higher energy (~0.879 eV). Unlike the PL, some of these spectra also show several higher-energy peaks corresponding to higher-order QW transitions (e.g., samples B and C).

Figure 5 displays the ER modulus spectrum of the four samples in the energy region of the waveguide-core/barrier and InP substrate (higher-energy peak at ~1.35 eV). Samples A, B, and D were all designed to have an unstrained waveguide-core/barrier band gap (E_g) at ~1.1 eV, which is clearly the case for A and D (peaks at 1.109 and 1.120 eV, respectively), but sample B has an unexpectedly higher barrier E_g of ~1.144 eV. We surmize that this is because it was grown earlier in the sequence whilst compositions were being fine tuned. Since this results in a deeper QW, this explains the higher ground-state confinement energy observed in, e.g., the PL and SE (Figs. 2 and 3, respectively).[8] Though unintentional, the deeper QW in sample B might well act to improve carrier confinement in the device structures, in a somewhat similar way to that intended for sample C, which was deliberately designed with a wider band gap tensile barrier. As mentioned earlier, this was to improve device performance via the stronger confinement created by the higher barrier energy, and CB offset, and this should reduce carrier spillover effects and, consequently, the amount of Auger recombination.[9] As expected, sample C does indeed display two ER modulus peaks, from the unstrained waveguide core and tensile barriers (at 1.091 and 1.134 eV, respectively, see Fig. 5).

IV. THEORETICAL ANALYSIS OF THE WAVEGUIDE-CORE/BARRIER FRANZ–KELDYSH OSCILLATIONS ER SPECTRA

A measurement of E_g is useful in determining the actual waveguide-core/barrier composition, as compared to that intended. However, it should be noted that the use of modulus

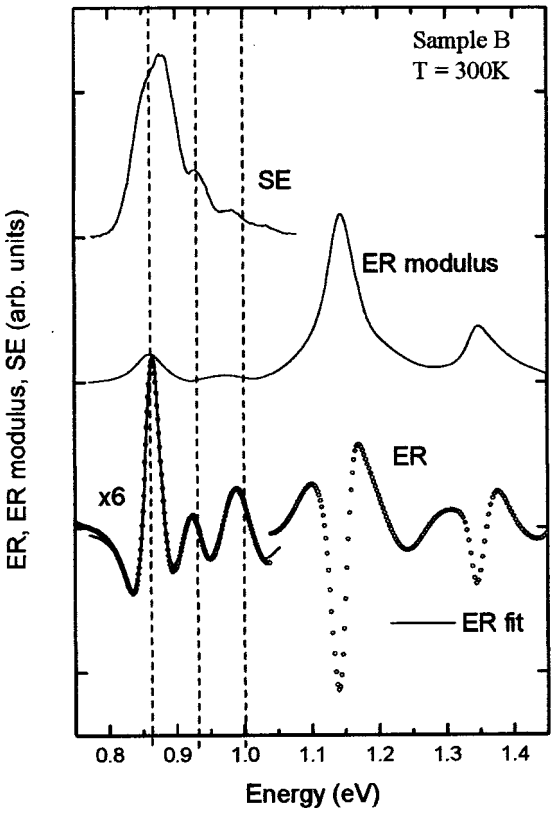

FIG. 4. Sample B typical room temperature spectra. For clarity, the base lines are offset as indicated by the ticks on the vertical axis. Lower plot: ER spectrum (circles). The QW region is magnified by a factor of 6 and fitted with a line shape model (solid curve), yielding fitted QW energies (0.863, 0.931, and 1.001 eV) represented by three vertical dashed lines. Middle plot: ER modulus spectrum for sample B obtained by Kramers–Kronig transformation of the ER spectrum in the lower plot. Top plot: SE spectrum for device fabricated from sample B.

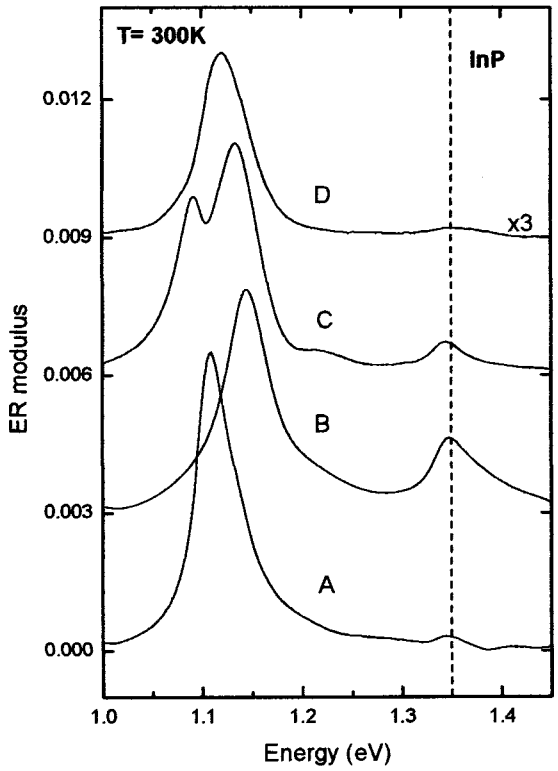

FIG. 5. Room temperature ER modulus spectra for the four samples A, B, C, D in the region of the barrier and substrate energies. For clarity, the base lines are offset vertically by multiples of 3×10^{-3} units. All spectra peak near 1.110 eV, except for sample B, which peaks at higher energy (1.144 eV). Sample C, which has a tensile barrier, displays two peaks from the tensile barrier and unstrained waveguide-core material. The highest energy peak, visible in all the samples, is due to the InP substrate band gap.

peaks to estimate transition energies has been shown to be formally correct only for a class of modulated reflectance profiles including confined-state QW transitions, and bulk-like features, which do not manifest Franz–Keldysh oscillations (FKO) characteristic of carriers being accelerated in the presence of appreciable built-in static electric fields ε_z.[5,6]

Here, however, we do in fact observe some FKO in the waveguide-core/barrier ER signals: the most obvious are in samples A (see Fig. 6) C and D. Hence, the earlier estimates of the waveguide-core/barrier band gap E_g from the modulus peaks in Fig. 5 must be treated with caution. The ER signals near E_g could, in principle, be a mixture of two: from the thick waveguide core and from the barrier layers between the QWs. However, we consider that the barriers are too thin (100 Å) to allow the carriers to be significantly accelerated, so suppressing any extended FKO and resulting in the simpler TDFF-like line shape localized in energy in the neighborhood of E_g (for which the modulus peak method *is* formally correct).[5,6] Any observed FKO above E_g must, therefore, originate from the thick unstrained waveguide core. This may, however, be mixed with any barrier TDFF line shape, potentially giving rise to a complicated overlapping spectrum. This is probably true for sample C which displays distinguishable barrier and waveguide-core signals of comparable amplitude (Fig. 5). Here, the barrier TDFF will be embedded in the high-energy oscillatory region of the waveguide-core FKO, resulting in a distortion of the FKO signal which will need special consideration. However, samples A, B, and D are designed to have the same (unstrained) barrier and waveguide-core composition, so the corresponding TDFF and FKO would have the same band gap energy E_g.

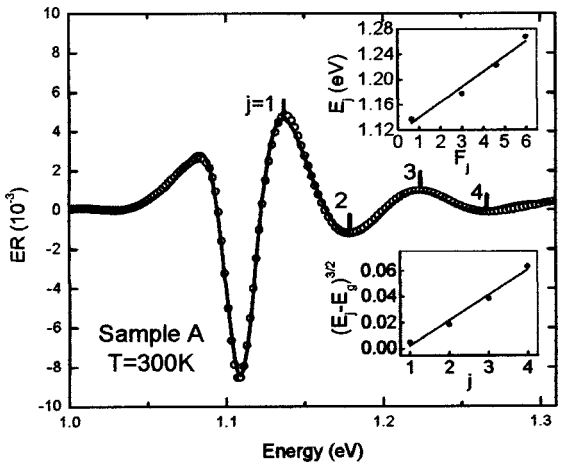

FIG. 6. The ER FKO spectrum in the energy range of the waveguide-core/barrier transitions (open circles) for sample A. The curve is a fit with the TDFF/Airy-function-based line shape model. The insets show final results from the combined Monte Carlo F_j- and j-plot techniques.

TABLE III. Summary of the results for all samples for the waveguide-core/barrier band gap energy (E_g), the electro-optic energy ($\hbar\Omega$) and built-in electric field (ε_z), obtained by analyzing the FKO in the ER spectra of the waveguide-core/barrier layers. The column headings indicate the method by which the results were obtained. The last three columns show the deduced values for ε_z. The figures in parentheses indicate the deduced uncertainties.

	Modulus	Airy-function fit		Fj plot		j plot		Average values		ε_z (kV/cm)		
											Poisson equation	
Sample	E_g (eV)	E_g (eV)	$\hbar\Omega$ (meV)	E_g (eV)	$\hbar\Omega$ (meV)	E_g (eV)	$\hbar\Omega$ (meV)	$\langle E_g\rangle$ (eV)	$\langle\hbar\Omega\rangle$ (meV)	FKO waveguide core	Waveguide core max	QW
A	1.109	1.107	26.8	1.116	24.1	1.108	25.9	1.110 (6)	25.6 (1.4)	102 (8)	108	16.5
B	1.144	1.141	38.7	1.141	33.4	1.139	33.8	1.141 (3)	35.3 (3.0)	167 (21)	98	17.0
C	1.091	1.080	30.9	···	···	···	···	1.085 (6)	30.9 (0.6)	134 (4)	114	15.5
	1.134	1.143	···	···	···	···	···	1.138 (7)	···	···	···	
D	1.120	1.118	26.5	1.113	20.0	1.110	21.0	1.115 (5)	22.5 (3.5)	84 (20)	106	16.5

As a result of these complications, we analyzed the waveguide-core/barrier ER signals in several alternative ways. The energy spacing of the semiperiodic FKO extrema (peaks and troughs—see, e.g., Fig. 6) can be related, in the usual way, to the electro-optic energy $\hbar\Omega$ of the accelerated carriers, which is in turn a measure of ε_z.[7] Here, we re-express the well-known relationship between $\hbar\Omega$, carrier reduced mass μ, and static field ε_z, as[10]

$$\varepsilon_z \approx 3.24\sqrt{\mu}\,(\hbar\Omega)^{3/2} \quad \text{with} \quad \frac{1}{\mu}=\frac{1}{m_e^*}+\frac{1}{m_h^*}, \tag{1}$$

where ε_z is in units of kilovolts per centimeter, μ in free electron masses (m_0), and $\hbar\Omega$ in milli-electron volts. Thus, provided the electron and hole effective masses, m_e^* and m_h^*, are known, analyzing FKO can also yield ε_z in addition to E_g. The built-in field is of interest in the present samples since it gives information about the doping profile of the structure.

There are several well-known methods of analyzing FKO to get E_g and $\hbar\Omega$ including fitting the full FKO line shape with a theoretical model based on Airy functions and their derivatives.[11,12] As mentioned earlier, the situation is complicated here by the potential presence of overlapping barrier and waveguide-core FKO signals. However, sample C has nondegenerate waveguide-core and barrier energies (see Fig. 5), and the ER can be unambiguously fitted with a line shape consisting of the sum of an Airy-based function (for the unstrained waveguide-core FKO) and a nondegenerate TDFF (for the tensile barrier). This fit also showed that the relative amplitudes of the waveguide-core and barrier signals are comparable, as indicated by Fig. 5. Hence, using this as a guide, the ER of samples A, B, and D was also successfully fitted with this model (but with the barrier and waveguide-core E_g now constrained to be equal). Table III shows the results obtained for E_g and $\hbar\Omega$ from the TDDF/Airy-function-based fitting. These fits also showed that the presence of an underlying TDFF, with the same E_g as the FKO, causes little distortion of the above-band-gap energy positions of the FKO extrema for samples A, B, and D. This allows the FKO of these samples to be analyzed separately by the well-known graphical methods, which we describe next.

The simplest method of obtaining $\hbar\Omega$ from the FKO involves plotting the energy positions of the above-band-gap extrema (see, e.g., Fig. 6) on an appropriate straight-line graph. This is based on the fact that, in the asymptotic region above E_g, the modulated reflectance signal can be shown to have the following approximate energy-dependence:[13]

$$\frac{\Delta R}{R}\propto \cos\left[\frac{2}{3}\left(\frac{E-E_g}{\hbar\Omega}\right)^{3/2}+\theta\right], \tag{2}$$

where θ is an (unknown) phase factor. This oscillatory expression has extrema at energies E_j given by

$$(E_j-E_g)^{3/2}=\tfrac{3}{2}(\hbar\Omega)^{3/2}(j\pi-\theta), \quad j=0,1,2,\ldots, \tag{3}$$

(The $j=0$ solution occurs only if $\theta<0$). This yields the first of the two possible graphical methods, which here we shall refer to as the "j-plot" technique:[10] the measured energies, E_j, of the peaks and troughs in the FKO (see, e.g., Fig. 6), are used to plot $(E_j-E_g)^{3/2}$ versus extremum index j, to yield a straight line whose gradient and intercept give $\hbar\Omega$ and θ, respectively. This method requires *a priori* knowledge of E_g. Here, unfortunately, we have only imprecise information on E_g (from, say, the modulus spectra in Fig. 5), which would therefore give an unacceptably large uncertainty in the resulting $\hbar\Omega$, [and thus, from Eq. (1), in ε_z].

On the other hand, when E_g is unknown, one may plot an alternative straight-line graph, given by re-expressing Eq. (3) as

$$E_j=\hbar\Omega(F_j)+E_g,$$

with

$$F_j=\left[\frac{3}{2}(j\pi-\theta)\right]^{2/3}$$

and

$$j=0,1,2.... \tag{4}$$

Thus, a linear plot of E_j vs F_j will yield $\hbar\Omega$ and E_g from the gradient and intercept, respectively. However, this method, here called the "F_j plot",[10] relies upon precise knowledge of the phase factor θ to allow the F_j factors in Eq. (4) to be determined (it also requires one to identify correctly the indices j of the extrema—which, since E_g is unknown, is not necessarily always obvious). It is known that θ depends on the dimensionality of the critical point[13] and is often assumed in the literature to be equal to $\pi/2$. However, it also depends on electron-hole interaction strength and short-range scattering processes[13] and, as we have pointed out earlier,[10]

also on sample conditions, layer optical thicknesses, and other essentially arbitrary factors. Thus, θ is actually usually completely unknown and could potentially have any value (between, say, $-\pi$ and $+\pi$). Allowing for such a range of possible θ in the F_j method would mean that, at best, only a range of possible values for $\hbar\Omega$ and E_g could be obtained.

Since our information on E_g is imperfect, while the phase factor θ is essentially unknown, the use of *both* the *j*-plot and F_j -plot techniques appears to be precluded. However, there is a route out of this dilemma using Monte Carlo techniques, as follows. The FKO signal amplitude is strongest near the band edge.[11] Thus, from the ER, and modulus spectra (Fig. 5), one can make a reasonable estimate of the *range* within which E_g is likely to lie (for instance, in Fig. 6, it is unlikely to lie above the first, $j=1$, extremum near 1.13 eV, nor below the small peak near 1.08 eV). If one makes a random guess of E_g, say E_{gj}, within such a likely range, one can then use the *j*-plot method [Eq. (3)] to estimate θ and the electro-optic energy, say $\hbar\Omega_j$. Then, using this estimate of θ, one can then employ the F_j-plot technique [Eq. (4)] to give estimates of the energy gap, say E_{gFj}, and electro-optic energy, say $\hbar\Omega_{Fj}$. We contend that, if the initial guess of E_{gj} was good, there should be a good agreement between this and E_{gFj}, and also between $\hbar\Omega_j$ and $\hbar\Omega_{Fj}$: i.e., the two graphical methods should agree well with each other. A measure of this agreement can be formed from the following factor:

$$\eta = \frac{|E_{gj} - E_{gFj}|}{1/2(E_{gj} + E_{gFj})} + \frac{|\hbar\Omega_j - \hbar\Omega_{Fj}|}{1/2(\hbar\Omega_j + \hbar\Omega_{Fj})}, \tag{5}$$

which should approach zero in the limit that the j and F_j plots give identical results for E_g and $\hbar\Omega$. Though this is unlikely to be achieved in reality, we argue that the smallest value that can be obtained for η by making a series of random Monte Carlo guesses for E_{gj} (within an acceptable energy range) gives the best possible compromise between the two graphical techniques. This scheme was adopted and a computer program written to make many random guesses ($\sim 10^5$) of E_{gj} within a given range, perform the appropriate *j*-and F_j-plot fits, calculate the respective values of $\hbar\Omega$, and keep track of the agreement factor η. The minimum value of η achieved (typically 10^{-2}) was assumed to represent the best possible scenario. The insets in Fig. 6 show typical final results from this technique (for the FKO of sample A, in which E_g was guessed in the range 1.06–1.12 eV).

Table III summarizes the results from analyzing the waveguide-core/barrier ER by the Monte Carlo F_j- and *j*-plot methods for samples A, B, and D (we consider that sample C could not be analyzed reliably by the graphical methods, because barrier signal is known to overlay the FKO in the crucial region above E_g). As may be seen, there is a good agreement with the other three methods employed (modulus spectra peak positions, and least-squares fitting of the FKO with the TDFF/Airy-function-based model).

The final stage in the analysis of the waveguide-core ER signals was to calculate the built-in electric fields ε_z, as follows. From the grand overall average value of E_g from the various techniques, $\langle E_g \rangle$, (see Table III), the waveguide-core quaternary composition was estimated from literature parameters (such as those in Ref. 14) assuming a lattice match to the InP substrate. From this composition, the quaternary electron and heavy hole masses (we assume that the light hole contribution to the FKO is negligible)[15] were calculated by linear interpolation in the [001] crystal direction (again using literature values, e.g., Ref. 14). Using the average value of the electro-optic energy, $\langle \hbar\Omega \rangle$, the final waveguide-core electric field ε_z was then calculated from Eq. (1) (see Table III).

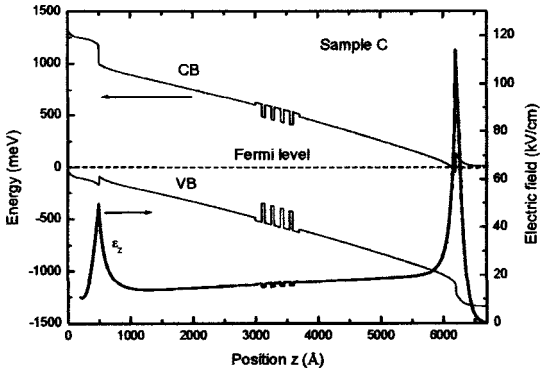

FIG. 7. The CB and VB profiles surrounding the relevant active region of sample C, (calculated by numerical solution of Poisson's equation, see Sec. IV). This shows the four 0.9% compressively strained QWs (50 Å) and five 0.28% tensilely strained barriers (100 Å), all sandwiched between two thick (2500 Å) unstrained InGaAsP waveguide-core, and InP cladding (500 Å), layers. The calculated electric field ε_z is $\sim$16 kV/cm across the QWs and a maximum electric field ($\sim$114 kV/cm) occurs at the deepest interface between the waveguide core and InP cladding. The results for samples A, B, and D are similar (see Table III), except that the QW barriers have the same band gap as the waveguide core.

In comparison to studies of similar structures,[10,16] the results for the waveguide-core/barrier electric fields in Table III are quite high: 102, 167, 134, and 84 kV/cm for samples A, B, C, and D, respectively. To corroborate these ε_z results, we performed a numerical solution of Poisson's equation following the method of Whiteaway,[17] in order to calculate the profiles of the CB and valence band (VB), and thus the expected built-in electric field throughout the structures. The samples are typical $p-i-n$ laser diodes in which there is a charge depletion layer between the *p*- and *n*-doped layers, giving rise to a nonuniform electric field across the active region of the device. We assumed that the dopant concentration is large enough ($\sim 5\times10^{17}\,\mathrm{cm}^{-3}$) that the built-in voltage is dropped virtually entirely across the undoped and comparatively highly resistive regions. This allows simplification of the structure modeled to that of only the waveguide-core/active region sandwiched between two 500 - Å -thick *p*- and *n*-doped InP layers. The model accounted for the layer thicknesses, band gap energies, CB and VB effective masses, CB offset relative to the adjacent layers, dopant concentrations, and static dielectric constants, as well as dopant binding energy, the latter being estimated using the usual Bohr hydrogenic model.[18] The Fermi level was assumed to be pinned at the surface, midway between the VB edge and acceptor level, some 23 meV above the VB edge. An example of a calculated band profile is given in Fig. 7, together with the resulting electric field (here for sample C).

It has been remarked that FKOs are often a measure of

the strongest electric field present in a structure, rather than the average.[19] Our observations confirm this interpretation: the analysis of the experimental FKO give large fields $\sim 100\,\mathrm{kV/cm}$ (see Table III) but the Poisson calculations show a markedly nonuniform electric field through the structures, with that in the majority of the waveguide core being only $\sim 16\,\mathrm{kV/cm}$. Large fields $\sim 100\,\mathrm{kV/cm}$ do occur, but only at the deeper waveguide-core/InP interface (see Fig. 7). As may be seen from Table III, there is a reasonable agreement between the maximum field in the Poisson calculations and that determined experimentally from the FKO. Thus, we conclude that the latter field pertains to the maximum, here at the deeper interface between the waveguide core and InP cladding layer. This conclusion is further confirmed by photoreflectance (PR) experiments on the same samples: in PR the observed FKO originate from waveguide-core/barrier material weighted through a different depth profile to that in the ER experiments, since attenuation of the pump laser (here, 1064 nm) means that material near the surface is much more strongly modulated in PR than that at depth. Since the fields at shallower depths are smaller ($\sim 10-50\,\mathrm{kV/cm}$, see Fig. 7), one would expect the PR to yield smaller fields for the FKO than those observed by ER, and this is, indeed, the case (fields of $\sim 36\,\mathrm{kV/cm}$).

V. THEORETICAL CALCULATIONS OF QW TRANSITION ENERGIES

In order to verify that the measured QW transition energies in the ER are as expected, given the layer widths and compositions, we used an eight-band $\mathbf{k}\cdot\mathbf{p}$ Hamiltonian to calculate the QW confined-state energies.[20,21] The basis states (each doubly spin degenerate) include the highest VBs (i.e., heavy hole, light hole, and spin-orbit split-off) and the lowest CB at $\mathbf{k}=0$. We quantize the Hamiltonian along the growth direction (z axis), perpendicular to the growth plane. For zero in-plane momentum ($k_x=k_y=0$), the $8\times 8\,\mathbf{k}\cdot\mathbf{p}$ Hamiltonian decouples into two independent 4×4 Hamiltonians, H, which we can use to determine the band edge energies in $In_{1-xw}Ga_{xw}As_{yw}P_{1-yw}/In_{1-xb}Ga_{xb}As_{yb}P_{1-yb}/InP$ heterostructures

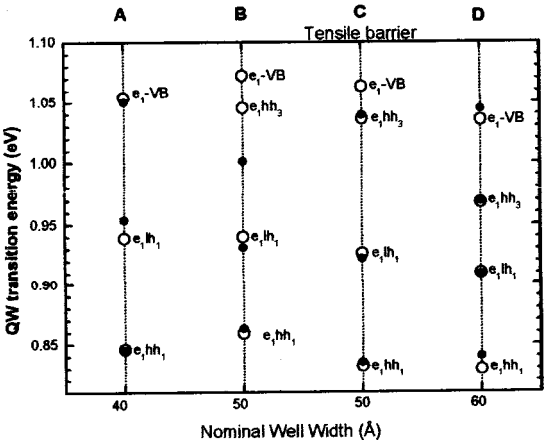

FIG. 8. QW energies obtained from ER line shape fitting (filled circles) and from theoretical calculations (open circles) for samples A, B, C, D.

$$H=\begin{pmatrix} E_{\mathrm{CB}}-e\varepsilon_z z & 0 & \sqrt{2}U & -U \\ 0 & E_{\mathrm{HH}}-e\varepsilon_z z & 0 & 0 \\ \sqrt{2}U^* & 0 & E_{\mathrm{LH}}-e\varepsilon_z z & Q \\ -U^* & 0 & Q^* & E_{\mathrm{SO}}-e\varepsilon_z z \end{pmatrix}, \tag{6}$$

where the subscripts CB, HH, LH, and SO stand for conduction, heavy-hole, light-hole, and split-off bands, respectively. U is the mixing between the CB and VBs at finite k_z, and Q the mixing between the light-hole and split-off band at finite k_z and strain. These matrix elements are functions of Ga-composition x, As-composition y, and in-plane strain ε_{xx}, as detailed in the Appendix. The tensilely strained barrier in sample C ($\varepsilon_{xx}=-0.28\%$) was explicitly accounted for. The additional $-e\varepsilon_z z$ terms in the diagonal elements of Eq. (6) describe effects of a uniform built-in electric field ε_z in the growth direction z, across the QW, where e is the electronic charge. This is included in order to calculate the magnitudes of the redshifts in the QW transitions associated with the quantum confined Stark effect (QCSE) in the present samples. However, using the results of the earlier Poisson calculations of ε_z present in the QW ($\sim 16\,\mathrm{kV/cm}$, see Fig. 7), the QCSE redshifts were found to be smaller than 0.2 meV, and therefore negligible.

Table I summarizes the final structural parameters used in the $\mathbf{k}\cdot\mathbf{p}$ calculation in order to obtain a reasonable match with those determined from fitting the ER. The barrier compositions used were those deduced, as described earlier, from the experimental values for the average barrier band edge $\langle E_g\rangle$ in Table III. For the QWs, we used the nominal concentrations and strain, allowing only their thickness, L_Z, to vary within the uncertainties of the TEM measurements (Table I). Tables I and II show the final values of L_Z used.

Figure 8 compares the final theoretical QW transitions (open circles) to the experimentally determined values (filled circles). Each vertical line in Fig. 8 represents one sample, the nominal well width of which is shown on the abscissa. Considering only parity-allowed transitions, all samples have two or more predicted possible confined QW transitions. Sample A, with the narrowest well, has two [e_1 to the first heavy hole state (hh_1) and e_1 to the first light hole state (lh_1)]. The other three samples have three

$(e_1hh_1, e_1lh_1, e_1hh_3)$. In two samples, A and D, we observed a higher energy feature in the ER that here we assign to a cross-interface transition from the QW first electronic state (e_1) to the VB of the barrier material. This can occur because the wells are quite shallow (in comparison, say, to longer-wavelength laser structures emitting at 1.55 μm). Any attempt at alternative assignments for this feature (such as parity-forbidden QW transitions, e.g., e_1hh_2, or cross-interface hh_1 to the barrier CB) substantially downgraded the agreement. For samples B and C, the high-energy $e_1 - VB$ transition is predicted to be very close to, and so effectively lost in, the very strong ER signal from the waveguide-core/barrier. From Fig. 8, there is generally an acceptable agreement between the ER and theoretical QW transition energies. The remaining differences are most likely due to residual uncertainties in layer compositions and the quaternary material parameters, especially for sample B, which, as remarked earlier, is further from growth specification than the other samples. Table II summarizes all the results obtained for the QW transition energies for all samples, from PL, SE, ER modulus spectra, least-square fitting of the ER spectra, and $\mathbf{k}\cdot\mathbf{p}$ theory.

VI. SUMMARY AND DISCUSSION

We have performed a comprehensive spectroscopic characterization of pieces of as-grown wafers of four different InP/InGaAsP/InGaAsP edge emitting lasers (A, B, C, and D) designed for high power Raman amplifier pump applications near 1450 nm, together with associated device studies. The designs included samples with different QW widths, as well as one (sample C) with tensilely strained barriers.

PL and ER measurements were performed on the four wafer pieces. The modulus of the ER spectra readily provided initial estimates of the energies of the ground state and several higher-order QW transitions, and the waveguide-core/barrier band gap. The estimates of the QW transition energies were refined by least-squares fitting to the ER spectra with a sum of TDFF oscillators. It was found that sample B had an unusually high QW ground-state transition energy. Preliminary SE measurements on devices provided corroboration for the PL and ER analyses of the prefabrication wafers.

The waveguide-core/barrier ER spectra revealed that sample B was unusual in another respect, in having a higher barrier band gap energy, E_g, suggesting slightly larger growth deviations in the waveguide-core/barrier composition in this sample. This results in a deeper well for this sample and thus greater confinement energy, thus explaining its higher-energy QW ground-state transition mentioned earlier. Sample C, on the other hand, was deliberately designed with a 0.28% tensilely strained barrier, in order to improve electron confinement and therefore device performance. The ER spectra confirmed this, resolving both the higher E_g in sample C, as well as the transition due to the lower-band-gap unstrained waveguide-core material.

Further analyses of the waveguide-core/barrier ER spectra confirmed the E_g obtained from the ER modulus spectra. These methods were: least-squares fitting of the waveguide-core/barrier ER spectra and/or; a thorough examination of the effectiveness of an approach to employing the two possible graphical methods of analyzing the FKO extrema (the F_j- and j-plot graphical techniques). Our proposed technique, which involves making Monte Carlo guesses of E_g within a reasonable range, allows E_g and the electro-optic energy $\hbar\Omega$, to be obtained graphically from the energy positions of the FKO extrema, even when there is no *a priori* knowledge of the parameters normally necessary (phase or E_g) for these standard graphical analyses. All methods produced consistent results for E_g and $\hbar\Omega$. The E_g results allowed the composition of the unstrained waveguide-core/barrier to be determined which, together with the results for $\hbar\Omega$, yielded the built-in static electric field. This field was compared with that predicted from a numerical solution of Poisson's equation for the structures, and was found to be of the same order as the maximum field, ~ 100 kV/cm, present in the structures (which is at the deepest waveguide-core/cladding interface).

The predicted field in the QWs was, however, much smaller, ~ 16 kV/cm, which had a negligible effect on the QW transition energies calculated by $\mathbf{k}\cdot\mathbf{p}$ theory (QCSE redshifts $< \sim 0.2$ meV). The predicted QW energies were compared to the ER fitting results, and a match was achieved by varying only the well widths in the model. From this we conclude that the actual QWs in samples B, C, and D are all somewhat wider than nominal (by 5, 3, and 10 Å, respectively) but within the tolerances indicated by TEM measurements. From these theoretical calculations, it was found that the highest-energy transition observed in the QW spectra occurs across the interface between the QW (e_1 ground state) and the barrier VB.

VII. CONCLUSION

This study confirms that ER is a potentially powerful tool that could be used for postgrowth characterization of Raman pump structures, giving an accurate and complete set of information, prior to actual device fabrication, about the QW thickness, waveguide-core/barrier compositions and built-in fields. In a follow-up study a comprehensive set of device characterization measurements on associated fabricated Raman pump lasers will be undertaken in order to gauge lasing performance and correlate this with the present spectroscopic findings. The overall aim is to determine which of the present, or possibly future, designs is best suited for high power Raman amplifier pump applications.

ACKNOWLEDGMENTS

The authors are grateful for the financial support of EPSRC (UK) and for providing a studentship for S. B. Constant. They are indebted to Dr. S. Ghosh and Dr. S. Choulis for invaluable advice on ER techniques, and to Iestyn Morris for advice on the Poisson calculations.

APPENDIX: DETAILS OF THE EIGHT-BAND k·p CALCULATIONS OF THE QW TRANSITION ENERGIES

The matrix elements in the Hamiltonian given by Eq. (6) vary with Ga and As composition x and y, and axial strain ε_{ax}, as follows:

$$E_{\mathrm{CB}} = E_{c0} + \frac{\hbar^2}{2m_0} s_c k_z^2, \tag{A1}$$

$$E_{\mathrm{HH}} = E_{v0} - \frac{\hbar^2}{2m_0}(\gamma_1 - 2\gamma_2)k_z^2 - \varepsilon_{\mathrm{ax}}, \tag{A2}$$

$$E_{\mathrm{LH}} = E_{v0} - \frac{\hbar^2}{2m_0}(\gamma_1 + 2\gamma_2)k_z^2 + \varepsilon_{\mathrm{ax}}, \tag{A3}$$

$$E_{\mathrm{SO}} = E_{v0} - \Delta_{\mathrm{so}} - \frac{\hbar^2}{2m_0}\gamma_1 k_z^2, \tag{A4}$$

$$U = \frac{1}{\sqrt{3}} P_0 k_z, \tag{A5}$$

$$Q = \sqrt{2}\,\frac{\hbar^2}{m_0}\gamma_2 k_z^2 - \sqrt{2}\varepsilon_{\mathrm{ax}}. \tag{A6}$$

Here $\gamma_1 = \gamma_1^L - E_p/(3E_g)$ and $\gamma_{2,3} = \gamma_{2,3}^L - E_p/(6E_g)$ are Luttinger parameters, $s_c = 1/m^* - (E_p/3)[2/E_g + 1/(E_g + \Delta_{\mathrm{so}})]$, Δ_{so} the spin-orbit splitting, $P_0 = \sqrt{2m_0 E_p/\hbar^2}$ is the Kane matrix element related to the Kane energy E_p, and $\varepsilon_{\mathrm{ax}} = -b_{\mathrm{ax}}(1 + 2c_{12}/c_{11})\varepsilon_{xx}$ describes the effect of axial strain on the VBs, with c_{11} and c_{12} as the elastic constants, b_{ax} as the axial deformation potential, and ε_{xx} as the in-plane strain. Literature sources were used for the material parameters (e.g., Refs. 14 and 22).

[1] Y. Emori and S. Namiki, Furukawa review **19**, 59 (2000).
[2] S. J. Sweeney, A. R. Adams, M. Silver, E. P. O'Reilly, J. R. Watling, A. B. Walker, and P. J. A. Thijs, Phys. Status Solidi B **211**, 525 (1999).
[3] S. Ghosh and T. J. C. Hosea, Rev. Sci. Instrum. **71**, 1911 (2000).
[4] A. F. Phillips, S. J. Sweeney, A. R. Adams, and P. J. A. Thijs, IEEE J. Sel. Top. Quantum Electron. **5**, 401 (1999).
[5] T. J. C. Hosea, Phys. Status Solidi B **182**, K43 (1994).
[6] T. J. C. Hosea, Phys. Status Solidi B **189**, 531 (1995).
[7] D. E. Aspnes, Surf. Sci. **37**, 418 (1973).
[8] Note that the SE spectrum of sample B (Fig. 3) also shows a weaker low-energy shoulder which is nearer to the (expected) QW band gap of the other three samples. If the barrier composition in sample B does indeed deviate significantly from nominal and there is further variation within the same (SE) sample, this might result in significantly inhomogeneous QW depths and band gaps. However, there is no evidence for such a doublet QW feature in any of the other QW spectra of sample B.
[9] S.J. Sweeney, T. Higashi, A. Andreev, A.R. Adams, T. Uchida, and T. Fujii, Phys. Status Solidi B **223**, 573 (2001).
[10] P. J. Hughes, B. L. Wiess, and T. J. C. Hosea, J. Appl. Phys. **77**, 6472 (1995).
[11] P. Y. Yu and M. Cardona, Fundamentals of Semiconductors, Physics and Material Properties, 3rd ed. (Springer, New York, 1999), Chap. 6.
[12] D.J. Hall, T.J.C. Hosea, and D. Lancefield, J. Appl. Phys. **82**, 3092 (1997).
[13] D. E. Aspnes and A. Studna, Phys. Rev. B **7**, 4605 (1973).
[14] I. Vurgaftman, J. R. Meyer, and L.R. Ram-Mohan, J. Appl. Phys. **89**, 5815 (2001).
[15] D Yan, F. H. Pollak, V. T. Boccio, C. L. Lin, P. D. Kirchner, J.M. Woodall, R.C. Gee, and P.M. Asbeck, Appl. Phys. Lett. **61**, 2066 (1992).
[16] G. Rowland and T.J.C. Hosea, J. Appl. Phys. **83**, 4909 (1998).
[17] J. E. Whiteaway, IEE Proc., Part I: Solid-State Electron Devices **130**, 165 (1983).
[18] J. R. Hook and H. E. Hall, Solid State Physics (Wiley, New York, 1991), Chap. 5.
[19] F.H. Pollak and H. Shen, Mater. Sci. Eng., R. **10**, 275 (1993), and references therein.
[20] A. T. Meney, B. Gonul, and E. P. O'Reilly, Phys. Rev. B **50**, 10893 (1994).
[21] E. P. O'Reilly, Semicond. Sci. Technol. **4**, 121 (1989).
[22] S.A. Choulis, T.J.C. Hosea, S. Tomić, M. Kamal-Saadi, A.R. Adams, E.P. O'Reilly, B.A. Weinstein, and P.J. Klar, Phys. Rev. B **66**, 165321 (2002).